Scratch iridescence: Wave-optical rendering of diffractive surface structure

SEBASTIAN WERNER*, Rheinische Friedrich-Wilhelms-Universität Bonn, Germany
ZDRAVKO VELINOV*, Rheinische Friedrich-Wilhelms-Universität Bonn, Germany
WENZEL JAKOB, École Polytechnique Fédérale de Lausanne (EPFL), Switzerland
MATTHIAS B. HULLIN, Rheinische Friedrich-Wilhelms-Universität Bonn, Germany

Fig. 1. Left: Inside of a cooking pot photographed under a halogen spotlight. Center and right: Renderings of scratched materials under environment lighting obtained using our model.

The surface of metal, glass and plastic objects is often characterized by microscopic scratches caused by manufacturing and/or wear. A closer look onto such scratches reveals iridescent colors with a complex dependency on viewing and lighting conditions. The physics behind this phenomenon is well understood; it is caused by diffraction of the incident light by surface features on the order of the optical wavelength. Existing analytic models are able to reproduce spatially unresolved microstructure such as the iridescent appearance of compact disks and similar materials. Spatially resolved scratches, on the other hand, have proven elusive due to the highly complex wave-optical light transport simulations needed to account for their appearance. In this paper, we propose a wave-optical shading model based on non-paraxial scalar diffraction theory to render this class of effects. Our model expresses surface roughness as a collection of line segments. To shade a point on the surface, the individual diffraction patterns for contributing scratch segments are computed analytically and superimposed coherently. This provides natural transitions from localized glint-like iridescence to smooth BRDFs representing the superposition of many reflections at large viewing distances. We demonstrate that our model is capable of recreating the overall appearance as well as characteristic detail effects observed on real-world examples.

CCS Concepts: • **Computing methodologies** → **Ray tracing**; **Reflectance modeling**;

*Joint first authors

This work was supported by X-Rite Chair and Graduate School for Digital Material Appearance. We thank Olesya Jakob for designing the door scene, and Clara Callenberg, Dennis den Brok, Julian Iseringhausen and Heinz-Christian Steinhausen for their feedback on the manuscript.

ACM Reference format:
Sebastian Werner, Zdravko Velinov, Wenzel Jakob, and Matthias B. Hullin. 2017. Scratch iridescence: Wave-optical rendering of diffractive surface structure. *ACM Trans. Graph.* 36, 6, Article 207 (November 2017), 14 pages.
https://doi.org/10.1145/3130800.3130840

1 INTRODUCTION

Modelling and rendering the real world with all its irregularities and imperfections remains one of the greatest challenges in computer graphics. A rich history of research on dirt, dust and fingerprints, weathering, patination, erosion [Dorsey et al. 2010] and scratches [Bosch et al. 2004; Dong et al. 2015; Merillou et al. 2001; Raymond et al. 2016; Yan et al. 2016] documents the massive amount of effort invested by our community to make computer graphics look less sterile and more realistic. In this paper, we focus on a subtle but very common effect observed on objects made of metal, glass or plastic. Under strongly directional lighting (like sunlight or a halogen spot), these surfaces exhibit colorful patterns that are caused by diffraction of light reflecting off microscopic surface details (Fig. 1). Being fundamentally a wave-optical phenomenon, this effect cannot be reproduced by geometric optics models and requires a careful study of both diffraction by individual surface features at the microscopic scale as well as interference among multiple features. The most detailed wave-optical simulations conducted in computer graphics thus far have involved detailed finite-difference time-domain (FDTD) modeling of periodic microstructures on butterfly wings [Musbach et al. 2013], an approach that is not feasible for structures beyond a few cubic micrometers.[1] In other works, the appearance

[1]For instance, FDTD simulation of light waves in a $1\,\mathrm{mm}^3$ volume would require $2.4{\times}10^{28}$ cell updates per second of simulated time ($\lambda = 500\,\mathrm{nm}$, grid resolution $\lambda/10$, time resolution $T/10$).

of large-scale diffractive objects has been approximated by combining far-field scattering models for repetitive microscopic structures with traditional texturing approaches. Most objects we interact with in our everyday use, however, exhibit features across many scales, ranging from macroscopic ones that are resolvable with the naked eye to microscopic ones that are only indirectly visible due to their aggregate interaction with light. This complexity leads to an intricate variation of appearance along the spatial, angular and spectral dimensions that no model so far has been able to express.

We propose a new spatially varying bidirectional reflectance distribution function (SVBRDF) modeling surfaces covered with microscopic scratch particles, which enables us to simulate scratch iridescence and contributes a first step to providing a framework for rendering such phenomena. Simulating the appearance of scratches within modern physically based rendering systems involves a number of challenges; for instance, traditional analyses of the diffracted wave field rely on a paraxial (small-angle) assumption that would lead to grossly inaccurate results in a BRDF model that must support evaluation for any pair of incident and outgoing angles. Our model thus simulates the diffraction of light by microscale surface features using a *non-paraxial* scalar diffraction theory proposed by Harvey [2000]. Our formulation leads to an SVBRDF with naturally coupled spatial, angular and spectral variation that exhibits multi-scale behaviour: at a distance, interference from a larger number of scratches causes it to resemble standard geometric optics models, while larger magnifications reveal iridescent reflections from small collections of scratches.

To model and simulate rough and scratched surfaces, we propose a vector graphics representation where an ensemble of fundamental primitives (linear scratch segments) resides on a base substrate. We show how the constituent scattering distributions can be expressed in closed form, and discuss automated and interactive techniques for placing large numbers of scratches on surfaces. Finally, we integrate our model into a modern physically-based rendering system and discuss efficient implementations of key operations, including importance sampling.

2 RELATED WORK

Detailed modeling and rendering of surface defects can dramatically improve the realism of renderings, hence the pursuit of such models has been a topic of great interest to the rendering community at large [Dorsey et al. 2010]. Early work in this area includes methods by Buchanan and Lalonde [1999] and Lu et al. [2000] who analyze general reflection properties of scratches. We group more recent related work into three main categories:

Explicit geometry. Merillou et al. [2001] and Bosch et al. [2008; 2004] derive BRDFs from the scratch cross-section (profile) at each shading point. Merillou et al. use a preset profile and texture mapping to position scratches, with scratch profiles split up into a number of tilted surfaces with associated procedural BRDFs. Bosch et al. enhance this model with generalized profile representations and curves on the surface of shaded objects to position scratches. Raymond et al. [2016] propose a multi-scale SVBRDF model based on a stack of coherently oriented scratch layers; their model relies on an accurate solution of interreflection within a scratch and supports multi-scale evaluation. All of these approaches separate spatial and optical information concerning the scratches, and their solutions only hold in the geometrical optics regime.

Microfacet models. BRDF models based on microfacet theory are widely used in graphics and have proven effective in reproducing the appearance of real-world materials [Ngan et al. 2005]. Here, we only focus on models that specifically target rendering of scratched surfaces. Yan et al. [2014; 2016] numerically integrate the normal distribution function (NDF) of normal-mapped surfaces over the surface region observed within a single pixel, which yields an efficient multi-scale reflectance model capable of rendering high-resolution normal maps under directionally peaked illumination. Dong et al. [2015] compare the use of microfacet and Kirchhoff scattering theory to predict surface appearance from the measured microgeometry of small surface patches. Also related to our work are image-based techniques that fit microfacet-based anisotropic reflectance models to measurements of finished wood [Marschner et al. 2005] or brushed metal surfaces [Dong et al. 2010; Wang et al. 2008].

Diffraction. Modelling diffraction by rough surfaces has been of great interest to the physics community and various models addressing the different characteristics of surfaces have been developed, ranging from Rayleigh-Rice vector perturbation theory (smooth surfaces) to more general ones such as Beckmann-Kirchhoff scattering theory (various roughness classes). A good overview as well as extensions of these scattering theories can be found in Krywonos [2006].

In the computer graphics community, a variety of BRDF models has been developed to account for diffraction effects created by microscale surface features in ray-based frameworks. However, none of them targets the transition between texture and far-field diffraction that is needed for our purpose. One of the first to incorporate wave-optical scattering theory into a BRDF model were Church and Takacs [2009]. Löw et al. [2012] later introduced their model to the graphics community and demonstrated its merits in numerical fits to measured reflectance data. He et al. [1991] derived a BRDF model based on vector Kirchhoff theory for surfaces with roughness described by a Gaussian random process. Stam [1999] proposed a BRDF model based on scalar Kirchhoff theory, that is capable of rendering the diffraction effects of randomly distributed primitives (e.g. rectangular bumps) or Gaussian random surfaces. The method relies on the power spectrum of the autocorrelation function of the surface height variations. Sun et al. [2000] derive an accurate far-field diffraction model to render compact discs modeled as a series of concentric tracks with a periodic arrangement of pits.

Cuypers et al. [2012] propose a Wave Bidirectional Scattering Distribution Function based on statistical optics, computing the Wigner distribution function of microstructures to produce solutions that are valid in the near- and far-field. This approach heavily relies on analytical solutions for regular structures, and it does not generalize to complex non-periodic microstructures due to the exceedingly high memory requirements associated with the underlying four-dimensional representation. More recently, Dhillon et al. [2014] developed a diffraction model based on heightfields acquired using an atomic force microscope; this data was used to generate look-up tables by truncating a Taylor-series expression of the BRDF. To better reproduce surface scattering effects based on statistical

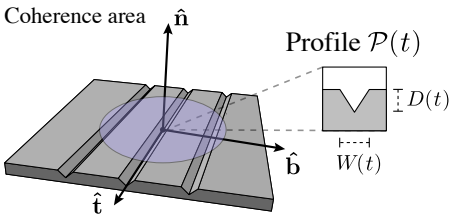

Fig. 2. Local shading geometry: Scratches that lie within the coherence area contribute to the diffracted radiance. We represent each scratch by a parametric curve $\boldsymbol{r}(t)$, which brings its own local coordinate system with tangent and bitangent directions $\hat{\boldsymbol{t}}(t)$ and $\hat{\boldsymbol{b}}(t)$, respectively. The cross-section at any position t along the scratch is defined by a profile $\mathcal{P}(t, b)$. We use profiles that lead to analytical Fourier transforms and scale them in the ($\hat{\boldsymbol{b}}$,$\hat{\boldsymbol{n}}$)-plane using parameters W (width) and D (depth)

properties of heightfields, Holzschuch and Pacanowski [2017] introduced the generalized Harvey-Shack theory to the computer graphics community. Lately, Belcour and Barla [2017] extended microfacet-based models to recreate thin-film interference. To acquire and render diffraction effects from planar surfaces at small angles, Toisoul and Ghosh proposed an efficient framework [2017]. Musbach et al. [2013] proposed a reflectance model for iridescent biological structures based on detailed FDTD simulation of vectorial wave propagation. This approach is significantly more general than the previously discussed models, but the prohibitive cost of this type of simulation limits it to periodic structures. Levin et al. [2013] use scalar Kirchhoff theory to predict BRDFs of a specific class of lithographically structured surfaces. While only remotely related to our work, their approach is one of the few to consider the effects of spatial coherence of the illumination source.

To overcome the discussed restrictions in the context of rendering scratched surfaces, our approach builds on an efficient representation tailored to this application. Similar to prior work [Bosch et al. 2004; Merillou et al. 2001], we separate spatial and optical information by describing the scratch layout as a curve and its reflectance behavior using a profile at each position along the curve. We use non-paraxial scalar diffraction theory [Harvey et al. 2000] to express the diffracted reflectance as a superposition of reflections from individual scratches. Similar to Sun et al. [2000] we derive the BRDF from the explicit calculation of the scattered complex wavefront, maintaining as much generality as possible. This allows us to take into account spatial coherence to reproduce not only diffraction effects but also the mutual interference created by dense scratch ensembles.

3 PRELIMINARIES

This section introduces the notation, geometric framework and relevant theory from prior work that serve as the foundation of our model. An overview of notation can be found in Table 1 .

3.1 Scratch representation

We represent a scratch as a curve $\boldsymbol{r}(t)$ parameterized by the arc length t, with local tangent vector $\hat{\boldsymbol{t}}(t) = d\boldsymbol{r}(t)/dt$. At any location t along the scratch, the surface normal $\hat{\boldsymbol{n}}(t)$, tangent $\hat{\boldsymbol{t}}(t)$ and bitangent $\hat{\boldsymbol{b}}(t) = \hat{\boldsymbol{n}}(t) \times \hat{\boldsymbol{t}}(t)$ form an orthonormal coordinate frame. The

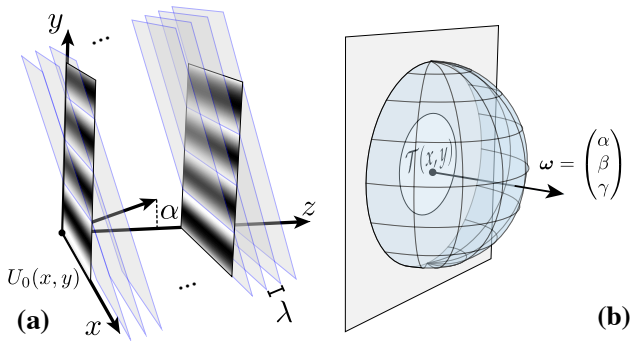

Fig. 3. (a), Angular spectrum. Viewed along slices perpendicular to the z-axis, a monochromatic plane wave traveling in direction (α, 0, $\sqrt{1-\alpha^2}$) causes vertical oscillations with frequency α/λ; translating the slicing plane incurs a corresponding phase shift. Using the Fourier transform, this relation can be used to express an arbitrary field $U_0(x, y)$ incident at $z = 0$ as a superposition of plane waves arriving from different directions. (b), We are interested in the far-field diffracted radiance $L(\boldsymbol{\omega})$, which is proportional to the squared amplitude of the plane wave traveling in the same direction.

Symbol	Meaning	Reference
$\boldsymbol{x}$, $\hat{\boldsymbol{x}}$	Vector, unit vector	
$\hat{\boldsymbol{\omega}}_i$, $\hat{\boldsymbol{\omega}}_o$	Incident and outgoing light directions	
Spatial parameterization		
$\boldsymbol{x} = (x, y)$	Position on z-plane	
$U(\boldsymbol{x})$	Scalar field amplitude	Sec. 3.2
$U_0(x, y)$	Scalar field in plane $z = 0$	Fig. 3a, Eq. 2
Plane-wave parameterization (spatial-frequency domain)		
(α, β, γ)	Vector of direction cosines	Fig. 3b, Sec. 3.2
$\boldsymbol{\xi}$	$(\hat{\boldsymbol{\omega}}_o - \hat{\boldsymbol{\omega}}_i)/\lambda$	Sec. 3.2
$\boldsymbol{\xi}'$	Projection of $\boldsymbol{\xi}$ in scratch frame	Eq. 11,13
Scratch representation		
t	Position along the scratch	
$\boldsymbol{r}(t)$	Point on scratch at position t	
$\{\hat{\boldsymbol{t}}, \hat{\boldsymbol{n}}, \hat{\boldsymbol{b}}\}(t)$	Local scratch coordinate frame (tangent, normal, bitangent) at t	Sec. 3.1, Fig. 2
b	Bitangential coordinate	
$\mathcal{P}(t, b)$	Scratch profile at t as function of b	
$W(t)$, $D(t)$	Scratch width and depth at t	
η	Spatial phase integral	Eq. 12, 23
k, (k)	Scratch index (for ensemble summation)	Eq. 9
λ	Optical wavelength	
$\mathcal{G}$	Gaussian spatial filter	Fig. 4c, Sec. 4.1
δ_c	Coherence area diameter, $\delta_c = 60\mu m$	Sec. 4.1
$\mathcal{T}(\boldsymbol{x})$	Optical transfer function	Fig. 3b, Sec. 3.2
A_s	Shading area	Eq. 2

Table 1. Overview of the notation used in this paper. The references point to the location where the quantity is introduced.

geometric cross-section of the scratch at position t is defined by the *profile* $\mathcal{P}(t, b)$, which specifies a 1-dimensional height profile along the bitangential coordinate b. Our model relies on scratch profiles that have analytical 1D Fourier transforms, such as rectangle or triangle shapes. Their scale in the ($\hat{\boldsymbol{b}}$,$\hat{\boldsymbol{n}}$)-plane is given by the width and depth parameters $W(t)$ and $D(t)$, respectively (Fig. 2).

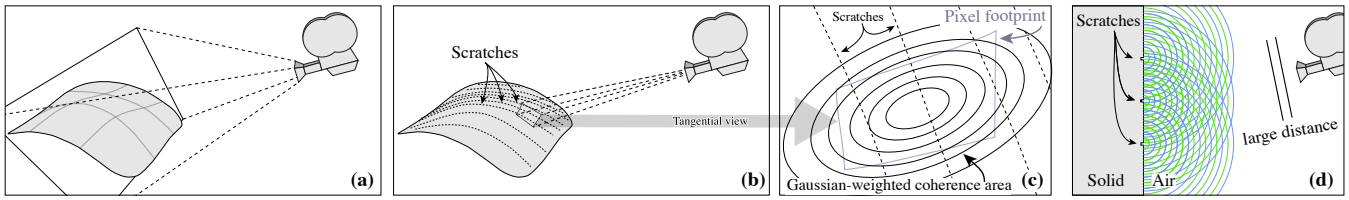

Fig. 4. From scratches to diffracted radiance: **(a)** Macroscopic view of a surface containing scratch particles. **(b)** Ray differentials establish a mapping between the visible surfaces and pixels of the output image. **(c)** Our method considers scratches located inside a Gaussian-weighted coherence region around the surface region covered by a pixel. **(d)** Side view: each scratch in the coherence region scatters the incident light into wavelets that interfere with each other; although not shown here, our method also accounts for reflection from the non-scratched base surface. Since the distance to the camera is much greater than the wavelength of light, it is enough to consider diffracted radiance, a far-field approximation of the superposition of wavelets that remains accurate for all angles of observation.

3.2 BRDF model

To quantify the interaction of light with a surface exhibiting microscale defects in physically-based rendering frameworks, we begin with the well-known definition of the bidirectional reflectance distribution function (BRDF)

$$f_r = \frac{dL_s(\boldsymbol{x}, \hat{\boldsymbol{\omega}}_o)}{dE_i(\hat{\boldsymbol{\omega}}_i)}, \tag{1}$$

which relates differential irradiance to scattered radiance. Here, $\boldsymbol{x}$ represents a position on the surface, $\hat{\boldsymbol{\omega}}_i$ is the direction from which this surface is illuminated and $\hat{\boldsymbol{\omega}}_o$ is the direction from which it is observed. To compute the radiance scattered by a diffracting aperture, we rely on a far-field approximation for scalar diffraction theory, known as *diffracted radiance*, which was introduced by Harvey et al. [2000]. It builds on tools from Fourier optics [Goodman 1996], specifically the *angular spectrum*, and is accurate in the far field and for diffracting apertures that are significantly larger than the wavelength of the radiation (both, far-field and aperture condition are satisfied by our application). Being part of a *scalar* theory of light transport, these two tools assume that the electromagnetic field can be described by the (scalar) amplitude of oscillations, as opposed to the commonly used vectorial electric and magnetic fields. Let $U(x, y, z)$ denote the scalar amplitude of the electric field at position $(x, y, z)^T$, and let $U_0(x, y) := U(x, y, 0)$ denote a planar slice at position $z = 0$ (here called the aperture plane, cf. Fig. 3). Harvey shows that the radiance diffracted by the aperture is obtained by computing $U(x, y, z)$ for $z > 0$, which is given by a Fourier transform of the complex amplitude $U_0(\boldsymbol{x})$. Assuming a homogeneously illuminated diffraction aperture, the diffracted radiance can be written as

$$L(\hat{\boldsymbol{\omega}}_o, \alpha_i, \beta_i) = \gamma_i \frac{\lambda^2}{A_s} \left| \mathcal{F}\left\{ U_0(x, y)\, e^{2\pi i(\beta_i y + \alpha_i x)} \right\}_{\alpha,\beta} \right|^2, \tag{2}$$

where $\hat{\boldsymbol{\omega}}_o = (\alpha, \beta, \gamma)$, $\hat{\boldsymbol{\omega}}_i = (\alpha_i, \beta_i, \gamma_i)$ and A_s being the shading area. Importantly, this expression remains valid even for oblique angles of incidence. The variables of this parameterization are referred to as *direction cosines* with $\gamma = \sqrt{1 - \alpha^2 - \beta^2}$. Spatial coordinates in the above expression are expressed in units of the wavelength λ. The complex wavefront $U_0(\boldsymbol{x})$ can be described by the modulation of the wavefront of the incident light $U_i(\boldsymbol{x})$ with the so-called *transfer function* $\mathcal{T}(\boldsymbol{x})$ [Goodman 1996; Lipson et al. 2010] of the diffracting plane:

$$U_0(\boldsymbol{x}) = U_i(\boldsymbol{x}) \cdot \mathcal{T}(\boldsymbol{x}). \tag{3}$$

Assumption	Reference
Diffracted radiance	
Far-field scattering	Sec. 3.2; Eq. 2
Spatial coherence	
Equal coherence condition for the full scene	Sec. 4.1
Intensity drops off towards edges of a light source	Sec. 4.1
Surface representation	
Homogeneous base material	Sec. 4.2; Eq. 9
Scratches	
No intersections (Sum of transfer functions)	Eq. 9
No self-shadowing/masking	–
Linear segments with constant profile	Sec. 4.3; Eq. 11
Spatial–spectral separability	Sec. 4.3; Eq. 11

Table 2. References to assumptions used by our model

Taking into account the assumption of homogeneous illumination ($U_i(\boldsymbol{x}) = U_i$), a change of variables enables us to rewrite the representation of the Fourier transform in a non-scaled coordinate system, which yields the BRDF

$$f_r(\boldsymbol{\xi}) = \gamma_i \frac{1}{A_s} \frac{1}{\lambda^2} \left| \mathcal{F}\left\{ \mathcal{T}(\boldsymbol{x}) \right\}_{\xi_{1,2}} \right|^2, \tag{4}$$

with

$$\boldsymbol{\xi} = \begin{pmatrix} \xi_1 \\ \xi_2 \\ \xi_3 \end{pmatrix} = \frac{1}{\lambda} \begin{pmatrix} \alpha - \alpha_i \\ \beta - \beta_i \\ \gamma - \gamma_i \end{pmatrix}. \tag{5}$$

A detailed explanation of these steps is provided in the supplemental material.

Equation 4 is the non-paraxial spectral BRDF for reflected light that is diffracted by a surface exhibiting microscale features represented by an optical transfer function $\mathcal{T}(\boldsymbol{x})$. Diffracted radiance shares similarities with the diffraction BRDF proposed by Stam [1999, Eq. 7]. Stam's model explicitly utilizes Kirchoff theory (i.e. tangent-plane approximation and the Huygens principle) whereas diffracted radiance can be derived solely from the angular spectrum of plane waves [Krywonos 2006]. However, both approaches offer equivalent formulations for the far-field approximation at hand (i.e. homogeneous illumination). For our application to render spatially resolved scratches, we rely on diffracted radiance as it provides a convenient way to describe the amplitude and phase changes induced by light-surface interaction via the optical transfer function.

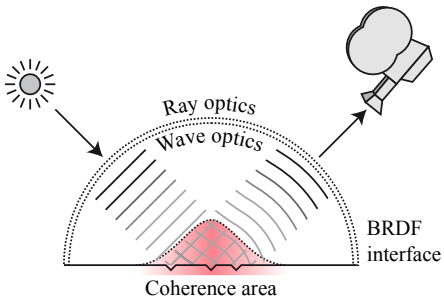

Fig. 5. To be compatible with a standard global illumination renderer, our model constrains wave optics to the reflectance model. The coherence area, represented by the Gaussian filter $\mathcal{G}$, marks the portion of the surface where scattered light waves will superimpose coherently. The interface to the outside world is provided in terms of geometric optics and radiance units. The computation of the coherence area is explained in Sec. 4.1

4 A DIFFRACTION SVBRDF FOR SCRATCHED SURFACES

The concept of ray tracing is fundamentally incompatible with the basic principles of wave optics. In fact, the wave-optical counterpart of a "ray" with sharply defined direction is a plane wave of infinite lateral extent and equal amplitude at each point on the sufficiently far away illuminated surface. Following Eq. 4, this leads to a Fourier transform of the whole surface regardless of its extent. Such an approach would be incapable of resolving localized surface features and would only be correct for point light sources or collimated beams. Since our goal is to create a model that permits resolving individual scratches affected by mutual interference, we draw on coherence theory to develop a physically justified interface between the long-range (ray-optical) light transport within a path tracing framework and the wave-optical scattering model. To this end, we will first introduce the concept of spatial coherence and use it to define a coherence window that will lead to a spatially varying BRDF (SVBRDF). We will then study the wave-optical contribution of a single scratch in isolation, and finally look at large ensembles of scratches.

4.1 Spatial coherence: resolving scratches

The van Cittert–Zernike theorem relates the angular extent of a light source illuminating a surface with a spatial filter on the surface via a Fourier transform [Goodman 1996; Lipson et al. 2010]. For instance, a point-light source yields a constant infinite spectrum whereas a disk-shaped area light results in an Airy function: this *coherence function* defines the corresponding spatial weights. More intuitively, it defines which structures in the vicinity of the observed point, such as scratches, actually contribute to the wave-optical scattering that leads to diffraction and interference. Usually, the distance between the first zero-crossings of the coherence function is used to define the *coherence area*, the extent of the filter. In the context of astronomy, a circular star of diameter $d = 0.07$ arcseconds e.g. has a coherence area of radius $r_c = 1.22\lambda/d \approx 1.9$m [Lipson et al. 2010]. After this first zero-crossing, the coherence function may predict further areas of coherence, which are suppressed if the light source is less intense around its edges. To approximate the coherence function, we make two simplifications: first, we assume that the same coherence condition holds throughout the scene, which allows us to define a global coherence function. Second, we will neglect coherence effects outside of the central peak, implicitly assuming a fall-off of the light-source intensity towards its corners. Similar to Dhillon et al. [2014], we define the coherence function as a spatial kernel $\mathcal{G}(\boldsymbol{x} - \boldsymbol{x}_0)$ controlling the relative weight of points on the surface with respect to the intersection point $\boldsymbol{x}_0$ of the ray on the surface. In contrast to Dhillon et al., who primarily introduce $\mathcal{G}$ to reduce the cost of discrete Fourier transformations used by their technique, our model requires coherence for its ability to resolve spatial surface structure. We model objects covered with an irregular arrangement of scratches, of which only a subset contributes to the light scattered within a pixel. Similar to a short-time Fourier transform, the kernel $\mathcal{G}$ provides a natural windowing function that performs this selection. This is a substantial difference to prior work modeling regular structures [Dhillon et al. 2014; Stam 1999]. We use the spatial kernel

$$\mathcal{G}(\boldsymbol{x}) = e^{-\frac{1}{2}|\boldsymbol{x}-\boldsymbol{x}_0|^2/\sigma^2}, \tag{6}$$

which is an isotropic Gaussian in the tangent plane around $\boldsymbol{x}_0$ (see Fig. 5). The coherence area diameter containing the salient portion of the footprint is defined as $\delta_c = 6\sigma$. We now modify Eq. 4 to account for spatial coherence:

$$f_r(\boldsymbol{x}_0, \boldsymbol{\xi}) = \gamma_i \frac{1}{A_s}\frac{1}{\lambda^2}\left|\mathcal{F}\left\{\mathcal{T}(\boldsymbol{x}) \cdot \mathcal{G}(\boldsymbol{x} - \boldsymbol{x}_0)\right\}_{\xi_{1,2}}\right|^2. \tag{7}$$

A common literature value for δ_c for scenes under direct illumination by sunlight or a light bulb in a kitchen environment [Divitt and Novotny 2015; Mandel and Wolf 1995] is $\delta_c = 60\,\mu$m, which we choose to approximate such illumination situations. Note that Eq. 7 behaves as previously discussed: for a point-light source, $\delta_c \to \infty$ and $\mathcal{G}(\boldsymbol{x}) \to const.$, reducing the SVBRDF to the BRDF of Eq. 4, which does not resolve surface features. On the other hand, an infinitely extended light source yields $\delta_c \to 0$, i.e. a Dirac delta coherence function.

In a practical rendering system, the intensity of a pixel in the rendered image will generally be computed as part of a stochastic ray tracing process, which samples the pixel footprint with a spatial reconstruction filter centered at $\boldsymbol{x}_0$. Our implementation converts these pixel sub-samples to real-valued radiance before averaging them, which maps to spatial coherence as the coherent subsamples are first converted to radiance and then incoherently superposed [Levin et al. 2013].

4.2 Additive composition of transfer function

We now turn to the Fourier transform of the optical transfer function, a key part of our model that we utilize to describe amplitude and phase changes of incident light waves induced by height variations of the shaded surface. We define $\mathcal{T}(\boldsymbol{x})$ as

$$\mathcal{T}(\boldsymbol{x}) = A(\boldsymbol{x}) \cdot e^{i\phi(\boldsymbol{x})} = \sqrt{F(\boldsymbol{x})} \cdot e^{i2\pi(\gamma_i+\gamma)h(\boldsymbol{x})/\lambda} \tag{8}$$

where $A = \sqrt{F}$ is the amplitude factor of the surface material, F is the Fresnel factor and $\phi(\boldsymbol{x}) = 2\pi(\gamma_i + \gamma_o)h(\boldsymbol{x})/\lambda$ is the change of phase induced by the height variation of the microstructure. As the optical path traveled by rays depends on the incident and outgoing

angle with respect to the surface normal, the optical path difference (and thus the phase change) exhibit a dependence on the view and light direction cosines γ_o and γ_i, respectively [Holzschuch and Pacanowski 2017; Krywonos 2006]. We now apply this concept to scratched surfaces, where each scratch is described by its individual transfer function. Here, the transfer functions encode local surface height variations, which change the phase of incident light waves that interact with the scratches. We assume our materials to consist of a homogeneous *base material* that does not exhibit spatial variation. This base material exhibits defects (scratches) at distinct positions. We model this by defining our transfer function as a base transfer function, from which we first subtract *masks* covering the defects and then add the defects back at the same position. This implies that masks and scratches must cover the same area on the surface. More formally,

$$\mathcal{T}(\boldsymbol{x}) = \mathcal{T}_{\text{base}}(\boldsymbol{x}) - \sum_k \mathcal{T}^{(k)}_{\text{mask}}(\boldsymbol{x}) + \sum_k \mathcal{T}^{(k)}_{\text{scratch}}(\boldsymbol{x}), \tag{9}$$

where the superscript (k) denotes the k^{th} mask-scratch pair and $\mathcal{T}_{\text{base}}(\boldsymbol{x}) = A_{\text{base}} = \sqrt{F_{\text{base}}}$. This decomposition of surface structure into individual scratches, and the additive superposition of their contributions is the key to a practical implementation of our model, since it allows for an efficient analytical evaluation of the Fourier transform in Eq. 4. The analytic evaluation also depends on two further simplifications: first, we assume the base to be a perfectly flat mirror, hence surface roughness would need to be emulated by an intractably dense distribution of scratches. Sec. 5 introduces an alternative mask-based blending scheme that combines our model with existing rough BRDFs based on microfacet theory. Secondly, we neglect scratch-scratch intersections, and our model consequently slightly overestimates the surface area of scratched portions of a surface. In a region where two scratches overlap, the base contribution will be subtracted (masked) twice and replaced by the sum of two scratches. For a correct handling of intersections, the full transfer function would be generated by a sum of height fields in the complex phase instead, which would not allow for our analytic solution. As we show in Sec. 6, the effect of this approximative handling of intersections can lead to a re-distribution of energy from the specular reflection towards higher order diffraction lobes. Note that as long as scratches and base have the same amplitude factor, this error only affects the diffracted phase but does not violate energy conservation. We provide an overview of all assumptions and simplifications used by our model in Table 2.

4.3 Single-scratch transfer function

The linearity of the Fourier transform allows us to first consider a single scratch transfer function (or its transform) and later extend the concept to a full solution. The local geometry of each scratch is defined by the profile $\mathcal{P}(t, b)$ (Sec. 3.1, Fig. 2), which is a 1-dimensional transverse scratch height profile defined in terms of the bitangent coordinate b. The resulting scratch-space optical transfer function takes on the following form in local coordinates:

$$\mathcal{T}_{\text{scratch}}(b, t) = A_{\text{scratch}}(b, t) \cdot e^{i2\pi(\gamma_i+\gamma)\mathcal{P}(b,t)/\lambda}, \tag{10}$$

where $A_{\text{scratch}}(b, t) = \sqrt{F(b, t)}$. The integral of the transfer function along the scratch length yields a spatial representation of the amplitude and phase changes induced by the material's height variations.

Incorporating the scratch profile. Considering its shift and rotation properties, the Fourier transform of a scratch transfer function can be understood as the integral over the Fourier transform of the rotated and shifted 1D transfer functions along the scratch trajectory, whose intricacy is determined by profile variation and curvature of the scratch. For simplicity, we consider scratches consisting of linear scratch segments whose profiles do not change along the segment. There is no loss of generality, as arbitrary curves of varying profile can always be split into linear segments of constant profile (and thus having a constant transfer function).

In addition, we assume only the spatial phases to be affected by the Gaussian filter, i.e., the width of a scratch is negligible in comparison to its length with respect to the coherence area. This allows us to separate the spatial (position) and spectral (profile) components of each scratch and to express its transfer function in the scratches' own tangent space with axes $\hat{\boldsymbol{t}}$, $\hat{\boldsymbol{b}}$ and $\hat{\boldsymbol{z}}$. The Fourier transform of a single scratch transfer function then reads

$$\begin{aligned} &\mathcal{F}\left\{\mathcal{T}_{\text{scratch}}(b, t)\right\}_{\xi'_{1,2}} \approx \\ &\mathcal{F}\left\{\mathcal{T}_{\text{scratch}}(b)\right\}_{\xi'_2} \cdot \int dt\, \mathcal{G}(t)\, e^{-2\pi i(\boldsymbol{r}'(t)\cdot\boldsymbol{\xi}')} = \\ &\left[\int db\, \mathcal{T}_{\text{scratch}}(b) e^{-2\pi i b \hat{\boldsymbol{r}}'_2 \xi'_2}\right] \cdot \eta \end{aligned} \tag{11}$$

where

$$\begin{aligned} \eta &= \int dt\, \mathcal{G}(t)\, e^{-2\pi i(\boldsymbol{r}'(t)\cdot\boldsymbol{\xi}')} \\ &= \int dt\, e^{-|\boldsymbol{r}'(t)|^2/(2\sigma^2)}\, e^{-2\pi i(\boldsymbol{r}'(t)\cdot\boldsymbol{\xi}')} \end{aligned} \tag{12}$$

and the projection into tangent space is given by the inverse of the rotation matrix defining the orientation of the scratch so that

$$\boldsymbol{x}' = \boldsymbol{R}^{-1}\boldsymbol{x} = \begin{bmatrix} — & \hat{\boldsymbol{t}}^T(t) & — \\ — & \hat{\boldsymbol{b}}^T(t) & — \\ — & \hat{\boldsymbol{z}}^T & — \end{bmatrix} \boldsymbol{x}\,;\; \boldsymbol{r}' = \boldsymbol{R}^{-1}(\boldsymbol{r} - \boldsymbol{x}_0) \tag{13}$$

and $\boldsymbol{r}'$ is the relative scratch position. With Eq. 11 at hand, we are now able to express arbitrary scratch profiles. This profile is incorporated into an optical transfer function that can be used to express the corresponding diffraction effects.

4.4 Scratch ensemble solution

We will now derive a general solution for surfaces with arbitrarily large scratch ensembles. Recall that Eq. 11 provided the Fourier transform of the transfer function $\mathcal{T}^{(k)}_{\text{scratch}}$ for an individual scratch observed in isolation. Substituting this expression into Eq. 9 yields the superposition of a general scratch ensemble. Because we assume a homogeneous material, the Fourier transform of the base transfer function $\mathcal{T}_{\text{base}}$ is given by the Fourier transform of the Gaussian filter kernel modulated by the square of the spatially uniform Fresnel coefficient (base amplitude). To compute the missing Fourier transform of the mask transfer function $\mathcal{T}^{(k)}_{\text{mask}}$, recall that scratches

and masks share the same locations on the surface. Thus, the respective integral over the spatial phases $\eta^{(k)}$ is the same and mask and scratch only differ in their respective profile. The mask is simply a part of the base material that was cut out. Therefore, $\mathcal{T}^{(k)}_{\text{mask}}(b)$ is equal to the base transfer function with $A_{\text{mask}}(b) = A_{\text{base}}$ without any phase deviations because no height variations are present, and its spatial extent is restricted to the scratch width. This yields the Fourier transform of a rectangular function

$$\begin{aligned}\mathcal{F}\left\{\mathcal{T}^{(k)}_{\text{mask}}(b)\right\}_{\xi_2'} &= \mathcal{F}\left\{A_{\text{mask}}\,\text{rect}\left(\frac{b}{W^{(k)}}\right)\right\}_{\xi_2'} \\ &= A_{\text{base}}\,W^{(k)}\cdot\text{sinc}\left(\pi W^{(k)}\xi_2'\right).\end{aligned} \tag{14}$$

We are now able to combine Eq. 11, Eq. 14 and Eq. 9 with Eq. 7 to get the Fourier transform of the scratched surface. We split the result into more intuitive base- and scratch related terms to obtain

$$f_r(\boldsymbol{x}_0,\boldsymbol{\xi}') = \gamma_i\frac{F}{\pi\sigma^2}\frac{1}{\lambda^2}\left|\mathcal{B}(\boldsymbol{\xi}') - \mathcal{S}(\xi_2')\right|^2, \tag{15}$$

where $A_s = \pi\sigma^2$ is the area under the squared amplitude of the Gaussian (shading area) and F the Fresnel coefficient of the homogeneous material. We define

$$\mathcal{B}(\boldsymbol{\xi}') = 2\pi\sigma^2 e^{-2\pi^2\sigma^2(\xi'^2_1+\xi'^2_2)}, \tag{16}$$

as the *base response* given by the Fourier transform of the filter kernel resembling the undisturbed reflectance of the material without scratches. On the other hand, the *scratch response*

$$\mathcal{S}(\boldsymbol{\xi}') = \sum_k\left[\mathcal{F}\left\{\mathcal{T}^{(k)}_{\text{mask}}\right\}_{\xi_2'} - \mathcal{F}\left\{\mathcal{T}^{(k)}_{\text{scratch}}\right\}_{\xi_2'}\right]\eta^{(k)}(\boldsymbol{x}_0,\boldsymbol{\xi}') \tag{17}$$

then defines the disturbance of the smooth heightfield by scratches. The scratch response thus relies on the scratches' profiles and their location on the surface with respect to the point of intersection encoded into the integral over the spatial phases $\eta^{(k)}$ (see App. A for the full solution). In its simplest form using a rectangular scratch profile (see App. B) and $A_{\text{mask}} = A_{\text{scratch}} = A_{\text{base}}$, the scratch response function is

$$\mathcal{S}(\boldsymbol{\xi}') = \sum_k \mathcal{W}^{(k)}\mathcal{D}^{(k)}\eta^{(k)}(\boldsymbol{x}_0,\boldsymbol{\xi}'), \tag{18}$$

$$\mathcal{W}^{(k)} = W^{(k)}\text{sinc}\left(\pi\frac{W^{(k)}}{\lambda}\xi_2'\right), \tag{19}$$

$$\mathcal{D}^{(k)} = \left(1 - e^{2\pi i(\gamma_i+\gamma)D^{(k)}/\lambda}\right), \tag{20}$$

where we further separate the dependence of the individual diffraction patterns of the scratches on the respective width and depth via the width-term $\mathcal{W}^{(k)}$ and the corresponding depth term $\mathcal{D}^{(k)}$. This constitutes our reflectance function for rendering surfaces with microscale scratches. In Sec. 5, we explain how our rendering system efficiently looks up the scratches that are relevant for a given shading event.

5 USAGE IN A RENDERING FRAMEWORK

In Sec. 4, we derived a BRDF for surfaces with micro-scale scratches that is compatible with standard ray tracing-based rendering systems. We use a standard backward path tracer that evaluates the BRDF at intersections found by tracing rays from the camera. The scratches are either applied to the surface by defining positions, directions, and other scratch parameters directly, e.g. by drawing them from a distribution, or by scratching an arbitrary mesh using an editing tool. In full-spectral rendering mode (all figures except Fig. 12), the renderer samples 16 wavelengths across the visible range. A reduced RGB version represents the primary colors by the wavelengths $\lambda_{\text{red}} = 700\,\text{nm}$; $\lambda_{\text{green}} = 520\,\text{nm}$ and $\lambda_{\text{blue}} = 440\,\text{nm}$.

Scratch data structure and lookup. The scratch particles are represented by line segments, which we store in a bounding volume hierarchy (BVH) consisting of axis-aligned bounding boxes (AABB). The BVH is built using sorting on a space-filling curve (Morton code builder [Lauterbach et al. 2009]) and efficient traversal is ensured by employing the skip-pointer structure proposed by Smits [1998]. To reduce spatial overlap between the elements of this structure, we perform further splits. Since the shading cost of our model generally outweighs the intersection test cost, we do not directly split the scratch particles. We instead use a directed acyclic graph structure, where multiple AABBs can be associated with the same leaf element and spatially subdivide the scratches into a number of elements that can be adjusted for performance improvements. During intersection testing, we store only the unique intersections within the shaded area. When shading a point on the surface, we only consider scratches within the pixel footprint. To achieve the correct incoherent superposition of the coherent subsamples for a given pixel, we need to integrate over the pixel footprint (cf. Sec.4.1). This ensures the right multi-scale behaviour and allows for spatial variation at the cost of a larger number of required samples per pixel compared to standard BRDF models. Rays that strike the surface at an oblique angle might query many scratch particles, leading to poor performance due to a large pixel footprint. However, note that scratches that lie outside of a sphere whose diameter equals the Gaussian filter kernel ($\Delta_c = 6\sigma = 60\mu m$) only have a negligible contribution, hence we limit the BVH query to the intersection of this sphere and the pixel footprint.

Importance sampling the base response function. To importance sample the base surface response Eq. 16, we generate two normally distributed samples and scale them by the standard deviation of the (Gaussian) target distribution in the angular spectrum, resulting in a sampled angular frequency $\boldsymbol{\xi}$. Specifically, we set

$$\boldsymbol{\xi}_{1,2} = [(\sqrt{8}\pi\sigma)^{-1}, (\sqrt{8}\pi\sigma)^{-1}]^T. \tag{21}$$

Next, the sampled frequency is used to map the incident direction onto a scattered direction $\hat{\boldsymbol{\omega}}_o = (\alpha_o, \beta_o, \gamma_o)^T$ by solving for α_o and β_o via $\alpha_i + \alpha_o = \xi_1$ and $\beta_i + \beta_o = \xi_2$, to obtain

$$\hat{\boldsymbol{\omega}}_o = \begin{pmatrix}\alpha_o\\ \beta_o\\ \gamma_o\end{pmatrix} = \begin{pmatrix}\xi_1 - \alpha_i\\ \xi_2 - \beta_i\\ \sqrt{1-\alpha_o^2-\beta_o^2}\end{pmatrix} \tag{22}$$

Two details must be noted regarding this step: occasionally, a sample satisfies $1 - \alpha_o^2 - \beta_o^2 < 0$, which does not lead to a valid

Fig. 6. We demonstrate our reflectance model on four example scenes. Top row from left to right: A golden door handle, a candle holder, both with randomized scratch distributions. A compact disc with circular scratches with constant separation. Bottom row: A spoon from different view points, the scratches are randomized. The top-down view reveals the scratches with iridescent colors that lie on a circle around the specular highlight. In the side-view the specular highlight only subtends a small fraction on the spoon and under incoherent illumination by the surrounding lights the scratches appear mostly white. At close-up again color as well as geometry of the scratches is revealed. We present complementary videos for these scenes in the supplemental material.

scattered direction. These samples correspond to evanescent waves that do not propagate, and the associated sample is simply dropped. Secondly, sampling a position in the angular frequency domain and mapping it on the outgoing hemisphere corresponds to a change of variables that appears both in the sampling density and Monte Carlo weight of this sampling strategy. The mapping is simply the parallel projection from the unit disc to the unit hemisphere known as the Nusselt analog, and the Jacobian determinant factor for the Gaussian PDF associated with this mapping is the direction cosine γ_o.

Importance sampling of the scratch response function. Importance sampling of the scratch response relies on a modification of a sampling technique that was originally developed by d'Eon et al. [2011] in the context of hair rendering. Given an incident direction (ϕ_i, θ_i) expressed in the coordinate system of a hair fiber, this technique works by sampling a specular reflection from an ideally reflecting cylinder, producing a reflected direction on a Dirac delta circle of azimuths with elevation angle $\theta_i = -\theta_o$. To account for roughness, the direction (ϕ_o, θ_o) is then perturbed by a random offset drawn from a spherical von Mises-Fisher distribution with concentration parameter κ. The spherical density of sampled directions has an explicit form in terms of a modified Bessel function of the first kind, specifically

$$p(\theta_o, \phi_o) = \frac{\kappa}{4\pi \sinh \kappa} e^{-\kappa \cos\theta_i \cos\theta_o} I_0 \left[\kappa \sin\theta_i \sin\theta_o\right]$$

Although disconnected from the explicit profiles of scratches, we found the resulting distribution to be an excellent match for the response function of individual scratches when interpreting the scratch tangent vector as a fiber direction and mirroring reflected directions that would enter the surface along the normal direction, doubling the density $p(\theta_o, \phi_o)$ for directions that lie in the upper hemisphere.

Our method applies multiple importance sampling via the balance heuristic [Veach and Guibas 1995] to combine sampling of the base surface and the weighted scratch profiles inside the coherence area into a single unified sampling strategy.

Combining other BRDFs with our model. It is of great importance to be able to combine different BRDFs to achieve generality. To this end, we developed a simple modified alpha-blending step that marries correct wave-optical shading and mutual interference of scratch contributions to (in principle) arbitrary base BRDFs. In our

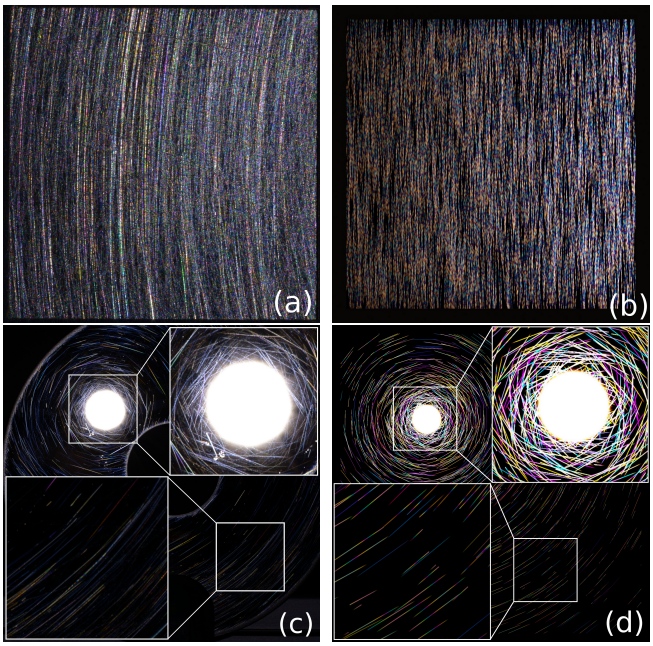

Fig. 7. Qualitative comparison between photographs of real-world scenes (a,c), and renderings of their digital recreations (b,d). We show a 2×2 cm^2 part of a heavily scratched metallic plate (a,b) and a more sparsely scratched metallic disc with 12 cm diameter (c,d). All surfaces have scratches in all orientations. However, they only become visible under the specular condition, which leads to concentric structures around specular highlights. From these examples, it becomes clear that the problem of fully recreating real-world surfaces is mostly related to complexity. The reference examples show great variation, and their roughness spans many scales which are currently not covered by our model.

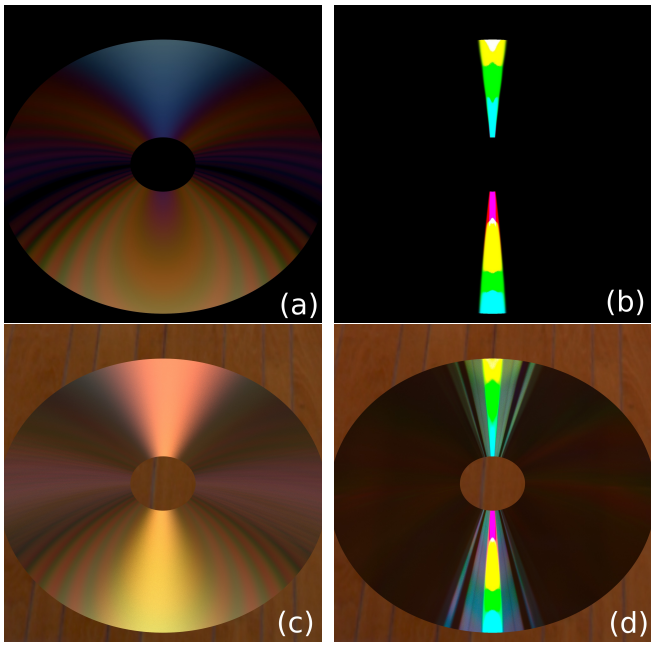

Fig. 8. Qualitative comparison between Stam's model (a,c) and ours (b,d) without (top) and with (bottom) environment light. The different representation of the CD surface structure by the two approaches leads to diverging appearance. Stams model treats CD surfaces as a (random) collection of bumps which re-distributes energy to higher order diffraction lobes visible over the whole disc. Our model, on the other hand, models CD tracks as uniform circular scratches which suppresses diffraction in parts not fulfilling the specular condition.

implementation, we use microfacet models to enable a rough base appearance even in unscratched regions. To achieve this goal, we first retrieve all the scratches from our BVH that fall into the coherence area as before. Next, we calculate the weighted scratch area density, i.e. the normalized sum of all contained scratch areas weighted using the Gaussian spatial filter. This yields a spatially varying ratio between the base and scratch contribution. We use this ratio to blend between the chosen base BRDF and our scratch SVBRDF (Eq. 15), setting the base response $\mathcal{B} = 0$ in Eq. 15 and $A_{\text{mask}} = A_{\text{scratch}} = 1$ to ensure energy conservation.

6 RESULTS

In this section we will first show example scenes rendered with our model to recreate the appearance of scratched surfaces. The corresponding render times and parameters can be found in the supplemental material. We will then discuss different aspects of our model in detail, including the impact of the coherent superposition of diffracted light, the possibilities to utilize and adapt our model to recreate realistic renderings and finally we will extend our model to incorporate not our specular base response function but an arbitrary microfacet model such as GGX [Trowbridge and Reitz 1975].

Scratching arbitrary objects. To facilitate authoring of assets, our editing tool allows the alteration of scratch particles in real time by drawing their spatial parameters from distributions or applying regular brush drawing techniques in 3D in combination with distribution based alterations of the optical (i.e. profile) parameters.

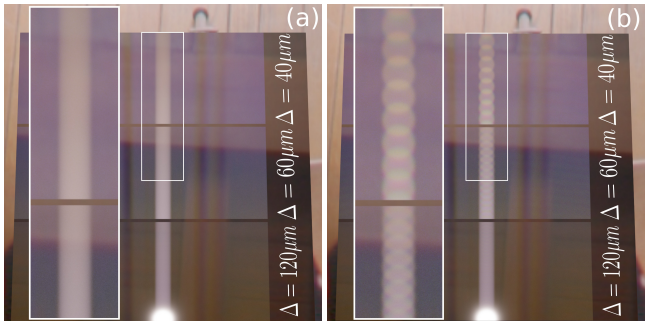

Fig. 9. Comparison of coherent and incoherent scratch diffraction superposition. The scratches lie on a metallic plate (GGX microfacet BRDF) and are horizontally arranged as three gratings with different separations Δ between the uniform scratches. Thus, we expect the diffraction orders only to be visible in vertical direction (across the scratches). (a): An incoherent superposition of scratches within the coherence area leads to colored scratches due to single-scratch diffraction. (b): A coherent superposition of scratches (our model) not only accounts for single-scratch diffraction but is also able to recreate mutual interference effects such as higher diffraction orders of the underlying scratch grating which reveals the separation of colors especially in the area of high intensity (see zoom-ins).

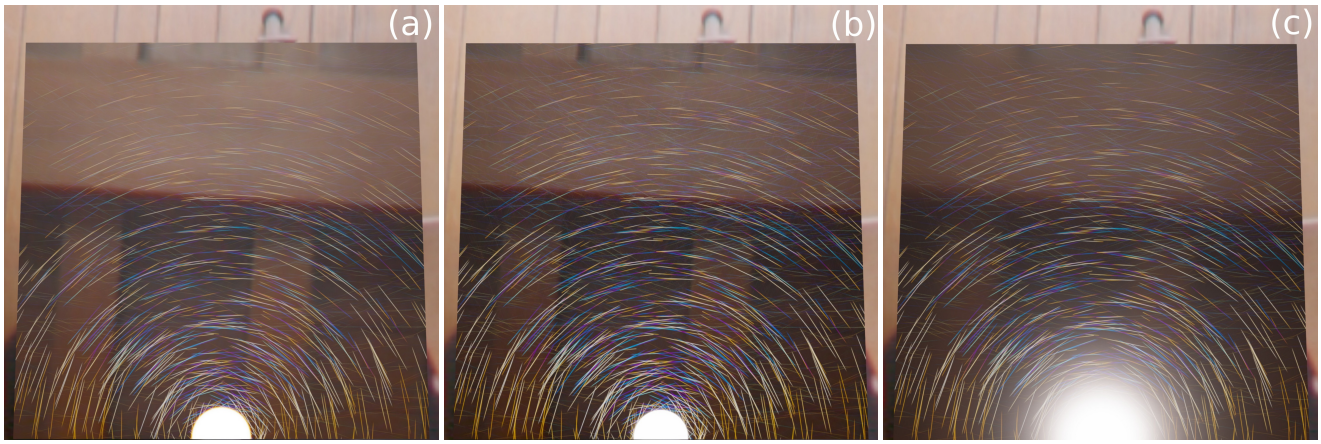

Fig. 10. Comparison of scratches on a plate with our coherent (a) base response, a smooth/specular GGX (b) and a rough GGX (c) base reflectance. We observe a change in color saturation as interference between base and scratches is neglected and single scratch diffraction is overestimated

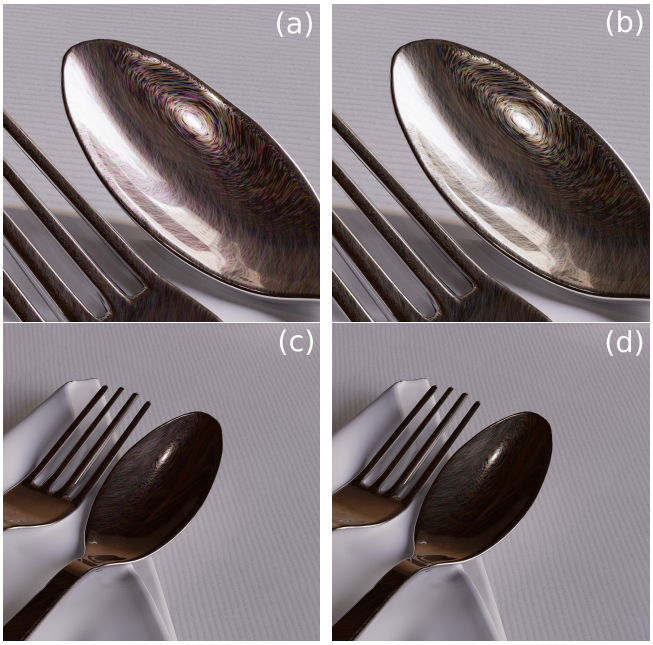

Fig. 11. Variation of scratch parameters greatly enhances the realistic appearance of our renderings. Subimages (a),(c): without variation; (b),(d): with variation along the scratches.

We provide a detailed video that showcases this tool in the supplementary material of this paper. Additionally, we have implemented tools that allow conversion of 2D vector graphics images to scratch particles by projecting them from texture to object space. In the editor, an approximate real-time BRDF model only shades the first intersected scratch with a single light sample; no coherent effects are taken into account.

Comparison to real-world data. To provide an intuitive comparison of effects our model is able to recreate, Fig. 7 compares photographs of real-world scenes and renderings of their digital recreations. Since the underlying surface structure is unknown, we restrict ourselves to a purely phenomenological comparison and use heuristics to distribute scratches and set their parameters. To focus on microscopic features, we compare photograph (macro-lens close-up) and rendering of a densely scratched metal plate (a,b) whereas the comparison of a scratched disc (c,d) places emphasis on the macroscopic properties. A common phenomenon in real-world scratches, the change of color along scratches due to varying profile (parameters), is closely reproduced by our model, whereas high-intensity glints in low-intensity regions are not since unscratched regions are black (smooth-surface assumption). The discrepancies most likely results from two features currently not covered by our model: additional base-surface roughness and inclined scratch normals resulting from a non-uniform scratching process, which leads to more complex scratch profiles. However, our model qualitatively reproduces scratch visibility according to the specular condition (tangent not perpendicular to projected light direction) forming circular structures around the specular reflection of the light source. Both examples illustrate that our model is capable of recreating the phenomenological features of diffractive scratches, which could likely be improved by stronger emphasis on the modeling step. A convenient step to introduce surface roughness for example could be to utilize our base-blending approach, described in the following, in combination with the scattering model proposed by Holzschuch and Pacanowski [2017].

Comparison to Stam's model. Most available reflection models that incorporate diffraction are restricted to single heightfield inputs or analytic solutions for periodic structures. For a qualitative comparison we provide renderings of a CD in Fig. 8. The periodic surface structure can be used by both, our approach (b,d) and the model proposed by Stam [1999] (a,c), though using different representations. Stam defines the surface as a periodic ensemble of *bumps* and computes the spectral power density as input for the BRDF. We, on the other hand, create tracks that consist of a number of scratches. Track separation and scratch parameters are taken from Stam [1999] so that the main difference between the two representations is that

ours does not account for gaps between scratches of one track. Both models diverge in appearance: Stam's model produces clearly visible higher order diffraction for tracks that do not fulfill the specular condition. The reason for this mainly lies in the surface representation: our model considers CD tracks as continuous scratches; the complex phasor defining the wave contribution (Eq. 15) is mainly driven by the scratch profile (and thus binormal direction). Stam's model, on the other hand, creates bumps of defined geometry which results in diffraction patterns in both, tangential and binormal direction. This leads to a (spectral) re-distribution of energy and therefore a change in color which is clearly visible in the upper row (area light only). The re-distribution of energy is emphasized in the bottom-row renderings (additional environment light) as it allows for the low-intensity higher order diffraction still to be visible. In contrast, our model is able to produce sparsely scratched surfaces such as shown in Fig. 7 where single scratches can be distinguished as well as the change of color along the scratch, a common phenomenon in non-manufactured real world scratches.

Coherent vs. incoherent superposition. The treatment of coherence is of great importance for effects such as mutual interference from structured surfaces, for example compact discs or holographic papers. Our model treats spatial coherence by applying a Gaussian weight to the contributions of scratches according to their position, as the complex diffracted amplitudes per scratch are superposed. Figure 9 reveals that without coherent superposition, effects such as diffraction orders generated by gratings are neglected and therefore the associated separation of colors cannot be reproduced. Our model on the other hand is able to closely reproduce such phenomena.

Profile variation. Scratches on surfaces are created by multiple effects such as every-day wear or even manufacturing. Whereas manufactured scratches or structures mostly have a well defined geometry, scratches produced by wear do not. To account for this and more closely reproduce such surfaces, we vary width and depth of scratch profiles by sampling from a simplex-noise function [Perlin 2002]. The random number generator used to generate the noise is seeded by the scratch index k to ensure determinism. This feature increases realism with very modest impact on performance and memory footprint, since longer scratch segments do not need to be split up to incorporate such variations. Figure 11 compares the effect of this parameter variation to scratches of constant parameters.

Microfacet base blending. In Fig. 10 we show results for our model with our simple blending approach in comparison to the coherent base response. Our fully coherent solution (a) shows good agreement with the specular GGX base (b) in terms of scratch colors and base reflectance. However, some changes are noticeable: first, the specular highlight of our model exhibits a red outline which is due to our separate treatment of wavelengths. Red light is scattered more strongly compared to smaller wavelengths, an effect which is not the case for geometrical optics models. Second, we observe more saturated colors, which results from the lack of interference with the base. Due to the neglected scratch-base interaction, we do not correctly account for the re-distribution of energy and we overestimate the energy diffracted by the scratches. The use of different microfacet models allows us to incorporate surface roughness (c)

Fig. 12. Our editing tool allows us to map complex scratch patterns onto objects of our choice. Here we "engraved" a ring and a planar surface with an intricate vector pattern (inset). Depth and width were drawn from a Gaussian distribution.

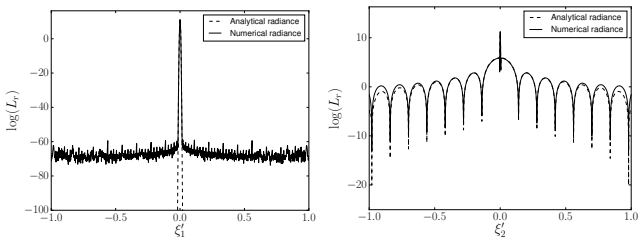

Fig. 13. Comparison of numerical and analytical slices of the radiance distribution for a single scratch (Fig. 14 left). Left;$\xi_2' = 0$: The slice in tangential direction of the scratch reveals the impact of the Gaussian filter. Right;$\xi_1' = 0$: The radiance distribution in bitangential direction shows the characteristic diffraction pattern. Our model greatly enhances performances as the analytic solution exhibits a computational complexity of $O(NM)$ for a single scratch opposed to $O(NM \log(NM))$ for the FFT.

which, by construction, does not affect the scratches but only the base response. In this way we are able to retain the iridescent effects of scratched surfaces with only minor differences and utilize the benefits of microfacet models.

Mapping complex scratch patterns. Our editing tool also allows us to project (in principle) arbitrarily complex scratch patterns provided as vector graphics onto complex objects. Fig. 12 shows the mapping of a vectorized leaf-texture onto a ring and a plate.

Approximation evaluation. To evaluate the impact of our assumptions regarding separability (we discard the Gaussian filter in bitangential direction) and scratch-scratch intersections, we compare the numerical radiance obtained via FFT against our model. To this end, we create surfaces which exhibit a number of scratches and rasterize these. The resulting heightfield (including scratch intersections) is used to create an optical transfer function via Eq. 8 and then input into the FFT. The radiance is obtained according to Eq. 7 with unit amplitude and the origin as the intersection point. We first show the radiance corresponding to a surface with a single scratch with tangent $(1, 0, 0)$ (Fig. 13 and Fig. 14(left)) to clarify single aspects of our approximation and problems that arise when using the FFT. A slice along the scratch (left, ξ_1' is the direction cosine in tangential direction) reveals a paraboloid function that rapidly drops off as is

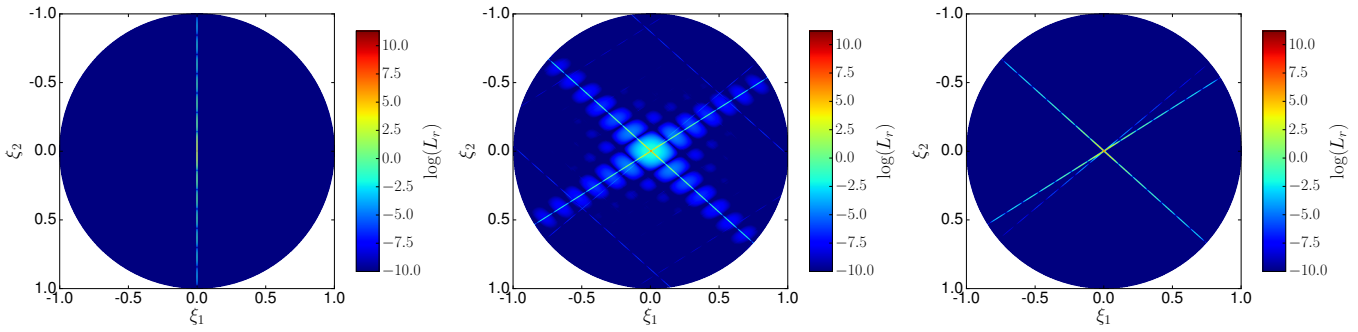

Fig. 14. Numerical radiance obtained via FFT vs. our Model in direction cosine space. Left: Analytic single scratch radiance in direction cosine space. Middle; Right: A surface with 10 randomly distributed scratches. The numerical solution for the whole hemisphere (middle) shows ghosting artifacts as well as parallelogram-shaped structures of low intensity (PSNR=84.9 dB) which are not present in our analytic model (right). The former result from the discretization of the heightfield whereas the latter correspond to the neglected intersections of scratches within the coherence area. All plots are available in the supplemental material in high resolution. Additionally, plots for different discretization resolutions are available to emphasize the difference between ghosting and assumption impact.

expected for a Gaussian in logarithmic representation. We expect a Gaussian as the scratch is longer than the surface we consider, therefore extending the integration limits for $\eta^{(k)}$ to $(-\infty, \infty)$. This behavior is reproduced by our model and in good agreement with the numerical solution. A slice across the scratch (right, ξ_2' corresponds to the bitangential direction) reveals the effects of an approximation in our model: since we neglect the convolution with the Gaussian filter in the bitangential direction (cf. Eq. 11), the radiance is underestimated for larger angles. Interpreting the convolution as a re-distribution of the diffracted energy, it should decrease the central peak while increasing the side lobe maxima. Taking these limitations into account, our model agrees well with the numerical results. For a surface with ten randomly distributed scratches (Fig. 14), the numerical solution for the whole hemisphere (middle) shows discretization-related ghosting artifacts, which are not present in our analytic model (right). Additionally, parallelogram-shaped structures are visible in the numerical solution that result from scratch-scratch intersection. Although of comparably low intensity (PSNR=84.9 dB) these correspond to a re-distribution of energy from the main- and side-lobes of the diffraction pattern to the parallelogram structures and thus, together with our approximations (see single scratch), can lead to an overestimation of higher order diffraction lobes resulting in overly saturated scratch colors. However, scales and primary (i.e. non-artifact) radiance distributions agree well, especially along the bitangential directions of the scratches, which reveals the characteristic diffraction distribution. Note that the analytical model delivers a significant performance increase as the computational complexity is only $O(NM)$ for a single scratch in comparison to $O(NM \log(NM))$. Precomputation would furthermore require a 4D lookup table with large memory footprint to sufficiently sample the spatial (Gaussian filter kernel) and spectral dimensions (FFT).

7 DISCUSSION AND FUTURE WORK

In this paper, we presented a wave-optical SVBRDF model for surfaces with iridescent microscale scratches. Our model encapsulates wave-optical computations in the shading evaluation and accounts for diffraction and mutual interference involving multiple scratches under a arbitrary viewing and lighting conditions. By approximating the spatial coherence using a Gaussian filter, we are able to recreate both localized glint-like iridescence and higher orders of diffraction from grating-like structures. Our approach is flexible on both the model and the data side: by subdividing paths on the surface into line segments and analytically calculating the associated diffracted complex amplitudes, we can support arbitrary scratch profiles. Furthermore, the separation of the spatial (paths) and optical (profiles) components enables efficient control of parameters and even spatial variation of parameters along scratches. Additionally, our editing tool allows us to freely scratch arbitrary geometries and apply complex scratching patterns with ease. Our model has the following limitations that could be addressed in future work:

Footprint integration. Our model subsamples the pixel footprint with a spatial filter resembling the coherence function to recreate local wave-optical diffraction. For full convergence, we rely on Monte-Carlo integration performed by the ray-tracer. In future work, an important step to improve performance would be to approximate the integral of the coherent SVBRDF over the pixel footprint to create a full multi-scale model.

Importance sampling. Accurate sampling strategies for both, our base response functionas well as for microfacet models used for our base-blending readily exist. The sampling strategy for the scratch response function samples the azimuthal direction uniformly [d'Eon et al. 2011], which is overly conservative considering for example the sinc-distribution (cf. Eq. 21 for the square profile. In future work, more efficient sampling schemes for typical diffraction patterns and, more challenging, mutual interference of scratch ensembles could be developed.

Other scratch profiles. We only presented results for a rectangular profile function, showing that it is expressive enough for recreating such intricate effects as iridescent scratches. Additional renderings of rectangular and triangular profiles in comparison can be found

in the supplemental material. We expect to obtain a wider variety of scattering distributions from different scratch profiles, leading to an increased degree of realism. Both, profiles with analytic solutions (like V-shaped or Gaussian grooves) as well as tabulated scattering distributions for arbitrary scratch profiles could be precomputed and used at moderate additional cost.

BSDF extension. So far, we showed that our model is able to represent the reflection properties of scratched surfaces. On the other hand, the scattered radiance of our SVBRDF is only dependent on the difference between the incident and outgoing directional cosines. This implies that the model in principle generalizes to transmittance effects (thin materials without internal scattering, like foils or very light curtains) via a simple sign change. This would be an interesting avenue to explore, as many real world diffraction effects are observed in transmittance rather than reflectance.

Coherent base - Use NDF to generate base height variation. Using our base-blending scheme we can in principle use arbitrary BRDFs as a base material. This approach does not account for phase variations that are directly produced by the surface roughness of the unscratched material. A future direction would be to derive a modified *coherent* base response function that is driven by surface roughness, for instance in the form of microfacet models.

Comparisons against real-world material samples. Given real-world data, both, experimental validation of our model and fitting of model parameters remains a major challenge due to the large number of unknowns involved. As of now, it is not yet clear what kind of input data would be needed to provide sufficient constraints, how to acquire such data, how to represent the surface (individual scratches or distribution parameters) and how to determine the model parameters in finite time. We look forward to studying these aspects in more detail in the future.

REFERENCES

Belcour, L. and P. Barla. 2017. A Practical Extension to Microfacet Theory for the Modeling of Varying Iridescence. *ACM Transactions on Graphics* 36, 4 (July 2017), 65. https://doi.org/10.1145/3072959.3073620

Bosch, C., X. Pueyo, S. Merillou, and D. Ghazanfarpour. 2008. A Resolution Independent Approach for the Accurate Rendering of Grooved Surfaces. *Computer Graphics Forum* (2008). https://doi.org/10.1111/j.1467-8659.2008.01342.x

Bosch, C., X. Pueyo, S. Mérillou, and D. Ghazanfarpour. 2004. A Physically-Based Model for Rendering Realistic Scratches. *Computer Graphics Forum* 23, 3 (2004), 361–370. https://doi.org/10.1111/j.1467-8659.2004.00767.x

Buchanan, J. W. and P. Lalonde. 1999. An Observational Model for Illuminating Isolated Scratches. *Proc. Western Computer Graphics Symposium 1999 (SKIGRAPH'99)* (1999).

Church, E. L. and P. Z. Takacs. 2009. Surface scattering. In *Handbook of Optics*, Bass, M. et al. (Ed.). McGraw-Hill, Chapter 7, 7.1–7.14.

Cuypers, T., T. Haber, P. Bekaert, S. B. Oh, and R. Raskar. 2012. Reflectance Model for Diffraction. *ACM Trans. Graph.* 31, 5, Article 122 (sep 2012), 11 pages. https://doi.org/10.1145/2231816.2231820

d'Eon, E., G. Francois, M. Hill, J. Letteri, and J.-M. Aubry. 2011. An Energy-Conserving Hair Reflectance Model. *Computer Graphics Forum* 30, 4 (2011).

Dhillon, D., J. Teyssier, M. Single, I. Gaponenko, M. Milinkovitch, and M. Zwicker. 2014. Interactive Diffraction from Biological Nanostructures. *Comput. Graph. Forum* 33, 8 (dec 2014), 177–188. https://doi.org/10.1111/cgf.12425

Divitt, S. and L. Novotny. 2015. Spatial coherence of sunlight and its implications for light management in photovoltaics. *Optica* 2, 2 (Feb 2015), 95–103. https://doi.org/10.1364/OPTICA.2.000095

Dong, Y., J. Wang, X. Tong, J. Snyder, Y. Lan, M. Ben-Ezra, and B. Guo. 2010. Manifold Bootstrapping for SVBRDF Capture. *ACM Trans. Graph. (Proc. SIGGRAPH)* 29, 4 (2010), 98:1–98:10.

Dong, Z., B. Walter, S. Marschner, and D. P. Greenberg. 2015. Predicting Appearance from Measured Microgeometry of Metal Surfaces. *ACM Trans. Graph.* 35, 1, Article 9 (Dec. 2015), 13 pages. https://doi.org/10.1145/2815618

Dorsey, J., H. Rushmeier, and F. Sillion. 2010. *Digital modeling of material appearance.* Morgan Kaufmann.

Goodman, J. 1996. *Introduction to Fourier Optics.* McGraw-Hill.

Harvey, J. E., C. L. Vernold, A. Krywonos, and P. L. Thompson. 2000. Diffracted radiance: a fundamental quantity in nonparaxial scalar diffraction theory: errata. *Appl. Opt.* 39, 34 (Dec 2000), 6374–6375. https://doi.org/10.1364/AO.39.006374

He, X. D., K. E. Torrance, F. X. Sillion, and D. P. Greenberg. 1991. A Comprehensive Physical Model for Light Reflection. In *Proceedings of the 18th Annual Conference on Computer Graphics and Interactive Techniques (SIGGRAPH '91).* ACM, New York, NY, USA, 175–186. https://doi.org/10.1145/122718.122738

Holzschuch, N. and R. Pacanowski. 2017. A Two-Scale Microfacet Reflectance Model Combining Reflection and Diffraction. *ACM Trans. Graph. (Proc. SIGGRAPH)* 36, 4 (2017), 66:1–66:12.

Krywonos, A. 2006. *Predicting Surface Scatter Using a Linear Systems Formulation of Non-paraxial Scalar Diffraction.* University of Central Florida. http://etd.fcla.edu/CF/CFE0001446/Krywonos_Andrey_200612_PhD.pdf

Lauterbach, C., M. Garland, S. Sengupta, D. Luebke, and D. Manocha. 2009. Fast BVH Construction on GPUs. *Computer Graphics Forum* (2009). https://doi.org/10.1111/j.1467-8659.2009.01377.x

Levin, A., D. Glasner, Y. Xiong, F. Durand, W. Freeman, W. Matusik, and T. Zickler. 2013. Fabricating BRDFs at High Spatial Resolution Using Wave Optics. *ACM Trans. Graph. (Proc. SIGGRAPH)* 32, 4, Article 144 (July 2013), 14 pages. https://doi.org/10.1145/2461912.2461981

Lipson, A., S. G. Lipson, and H. Lipson. 2010. *Optical physics.* Cambridge University Press, Leiden. https://cds.cern.ch/record/1338386

Löw, J., J. Kronander, A. Ynnerman, and J. Unger. 2012. BRDF Models for Accurate and Efficient Rendering of Glossy Surfaces. *ACM Trans. Graph.* 31, 1, Article 9 (Feb. 2012), 14 pages. https://doi.org/10.1145/2077341.2077350

Lu, R., J. J. Koenderink, and A. M. Kappers. 2000. Specularities on Surfaces with Tangential Hairs or Grooves. *Comput. Vis. Image Underst.* 78, 3 (jun 2000), 320–335. https://doi.org/10.1006/cviu.2000.0841

Mandel, L. and E. Wolf. 1995. *Optical Coherence and Quantum Optics.* Cambridge University Press.

Marschner, S. R., S. H. Westin, A. Arbree, and J. T. Moon. 2005. Measuring and Modeling the Appearance of Finished Wood. *ACM Trans. Graph. (Proc. SIGGRAPH)* 24, 3 (July 2005), 727–734.

Merillou, S., J. Dischler, and D. Ghazanfarpour. 2001. Surface scratches: measuring, modeling and rendering. *The Visual Computer* 17, 1 (2001), 30–45. https://doi.org/10.1007/s003710000093

Musbach, A., G. W. Meyer, F. Reitich, and S. H. Oh. 2013. Full Wave Modelling of Light Propagation and Reflection. *Computer Graphics Forum* 32, 6 (2013), 24–37. https://doi.org/10.1111/cgf.12012

Ngan, A., F. Durand, and W. Matusik. 2005. Experimental Analysis of BRDF Models. In *Proceedings of the Sixteenth Eurographics Conference on Rendering Techniques (EGSR '05).* Eurographics Association, Aire-la-Ville, Switzerland, Switzerland, 117–126. https://doi.org/10.2312/EGWR/EGSR05/117-126

Perlin, K. 2002. Improving Noise. In *Proceedings of the 29th Annual Conference on Computer Graphics and Interactive Techniques (SIGGRAPH '02).* ACM, New York, NY, USA, 681–682. https://doi.org/10.1145/566570.566636

Raymond, B., G. Guennebaud, and P. Barla. 2016. Multi-scale Rendering of Scratched Materials Using a Structured SV-BRDF Model. *ACM Trans. Graph.* 35, 4, Article 57 (July 2016), 11 pages. https://doi.org/10.1145/2897824.2925945

Smits, B. 1998. Efficiency Issues for Ray Tracing. *J. Graph. Tools* 3, 2 (Feb. 1998), 1–14. https://doi.org/10.1080/10867651.1998.10487488

Stam, J. 1999. Diffraction Shaders. In *Proceedings of the 26th Annual Conference on Computer Graphics and Interactive Techniques (SIGGRAPH '99).* ACM Press/Addison-Wesley Publishing Co., New York, NY, USA, 101–110. https://doi.org/10.1145/311535.311546

Sun, Y., F. D. Fracchia, M. S. Drew, and T. W. Calvert. 2000. Rendering Iridescent Colors of Optical Disks. In *Proceedings of the Eurographics Workshop on Rendering Techniques 2000.* Springer-Verlag, London, UK, UK, 341–352. http://dl.acm.org/citation.cfm?id=647652.732138

Toisoul, A. and A. Ghosh. 2017. Practical acquisition and rendering of diffraction effects in surface reflectance. *ACM Transactions on Graphics* (2017). https://doi.org/10.1145/3012001

Trowbridge, T. S. and K. P. Reitz. 1975. Average irregularity representation of a rough surface for ray reflection. *J. Opt. Soc. Am.* 65, 5 (May 1975), 531–536. https://doi.org/10.1364/JOSA.65.000531

Veach, E. and L. J. Guibas. 1995. Optimally combining sampling techniques for Monte Carlo rendering. In *Proceedings of the 22nd annual conference on Computer graphics and interactive techniques.* ACM, 419–428.

Wang, J., S. Zhao, X. Tong, J. Snyder, and B. Guo. 2008. Modeling Anisotropic Surface Reflectance with Example-based Microfacet Synthesis. *ACM Trans. Graph. (Proc. SIGGRAPH)* 27, 3 (2008), 41:1–41:9.

Yan, L.-Q., M. Hašan, W. Jakob, J. Lawrence, S. Marschner, and R. Ramamoorthi. 2014. Rendering Glints on High-resolution Normal-mapped Specular Surfaces. *ACM Trans. Graph. (Proc. SIGGRAPH)* 33, 4, Article 116 (July 2014), 9 pages. https://doi.org/10.1145/2601097.2601155

Yan, L.-Q., M. Hašan, S. Marschner, and R. Ramamoorthi. 2016. Position-normal Distributions for Efficient Rendering of Specular Microstructure. *ACM Trans. Graph. (Proc. SIGGRAPH)* 35, 4, Article 56 (July 2016), 9 pages. https://doi.org/10.1145/2897824.2925915

A GAUSSIAN WEIGHTED SPATIAL PHASES

The integration of the spatial phases of the scratches (and masks) relies on the following assumptions: First, the width of a scratch is negligible compared to its length with respect to the coherence area. Second, the scratch segments we integrate are lines. Third, the profile $\mathcal{P}$ does not change over a segment. To regain spatial resolution we apply a spatial filter kernel on the surface which weights each phase according to its position relative to the point of intersection (the origin of the footprint, see Fig. 2) and approximates the coherence function. This provides us with a closed-form solution of the integral of Eq. 11 given by

$$\eta^{(k)} = \int dt\, \mathcal{G}(t)\, e^{-2\pi i(\boldsymbol{r}'(t)\cdot\boldsymbol{\xi}')}$$

We represent our scratches as the relative position $\boldsymbol{r}'(t) = \boldsymbol{r}'_0 + t\cdot\hat{\boldsymbol{t}}' - \boldsymbol{x}'_0$; $t\in[-L/2, L/2]$ and $\boldsymbol{r}'_0(t) = \boldsymbol{r}'_0 - \boldsymbol{x}'_0$ where L is the length of the scratch and the prime denotes the coordinates in tangent space. The integral to solve then reads

$$\begin{aligned}\eta^{(k)} &= \int dt\, e^{-2\pi i(\boldsymbol{r}'(t))\cdot\boldsymbol{\xi}'}\, e^{-|\boldsymbol{r}'(t)|^2/(2\sigma^2)} \\ &= e^{-2\pi i \boldsymbol{r}'_0(t)\cdot\boldsymbol{\xi}'}\, e^{-\frac{|\boldsymbol{r}'_0|^2}{2\sigma^2}} \int dt\, e^{-2\pi i t\xi'_1}\, e^{-\frac{t^2+2t(\hat{\boldsymbol{t}}'\cdot\boldsymbol{r}'_{r,0})}{2\sigma^2}} \\ &= c_0\cdot\left[\operatorname{erf}\left(\frac{a_0+L/(2\sigma)}{\sqrt{2}}\right) - \operatorname{erf}\left(\frac{a_0-L/(2\sigma)}{\sqrt{2}}\right)\right]\end{aligned} \tag{23}$$

where L is the total length of the scratch and

$$\begin{aligned} a_0 &= 2\pi i\sigma\xi'_1 + \frac{(\hat{\boldsymbol{t}}'\cdot\boldsymbol{r}'_0)}{\sigma} \\ c_0 &= \sqrt{\pi/2}\,\sigma\, e^{h+if} \\ h &= -\frac{|\boldsymbol{r}'_0|^2}{2\sigma^2} - 2\pi^2\sigma^2\xi'^2_1 + \frac{(\hat{\boldsymbol{t}}'\cdot\boldsymbol{r}'_0)^2}{2\sigma^2} \\ f &= 2\pi\xi'_1(\hat{\boldsymbol{t}}'\cdot\boldsymbol{r}'_0) - 2\pi(\boldsymbol{r}'_0\cdot\boldsymbol{\xi}') \end{aligned} \tag{24}$$

B SCRATCH AND MASK PROFILES

We separate the spatial and the spectral component of the scratches which enables us to drive the reflection properties of a scratch by varying its 1d transfer function via the profile $\mathcal{P}_{\text{scratch}}(b)$. As we need to compute the Fourier transform of $\mathcal{T}_{\text{scratch}}(b)$ it is convenient to choose profile functions that lead to a closed-form solution and are drivable by the geometric parameters width W and depth D. We note that it would in general be possible to replace this function by a lookup table. The transfer function for a specific profile in general reads:

$$\mathcal{T}(b) = A(b)\, e^{-2\pi i(\gamma_i+\gamma)\mathcal{P}(b)/\lambda} \tag{25}$$

where $A(b)$ contains the Fresnel term and b is the bitangential coordinate in the $(\hat{\boldsymbol{b}},\hat{\boldsymbol{n}})$-plane (c.f. fig 2).

The mask transfer function $\mathcal{T}_{\text{mask}}(b)$ and its Fourier transform, given in Eq. 14, for a single scratch reads

$$\begin{aligned}\mathcal{F}\left\{\mathcal{T}_{\text{mask}}(b)\right\}_{\xi'_2} &= \mathcal{F}\left\{A_{\text{base}}\,\text{rect}\left(\frac{b}{W}\right)\right\}_{\xi'_2} \\ &= A_{\text{base}}\, W\cdot\text{sinc}\left(\pi W\xi'_2\right)\end{aligned} \tag{26}$$

which is always the case for the mask profile. On the other hand we are able to choose an arbitrary scratch profile. For simplicity we concentrate on two different profile functions which are driven by the scratches' widths and depths. The simplest case is a rectangular profile with constant depth, i.e.,

$$\begin{aligned}\mathcal{F}\left\{\mathcal{T}^{\text{rect}}_{\text{scratch}}(b)\right\}_{\xi'_2} &= \mathcal{F}\left\{A_{\text{scratch}}\,\text{rect}\left(\frac{b}{W}\right)\right\}_{\xi'_2}\Phi_D \\ &= A_{\text{scratch}}\, W\cdot\text{sinc}\left(\pi W\xi'_2\right)\Phi_D\end{aligned} \tag{27}$$

and depth-phase

$$\Phi_D = e^{-2\pi i(\gamma_i+\gamma)D/\lambda} \tag{28}$$

For triangular profiles, we obtain

$$\begin{aligned}&\mathcal{F}\left\{\mathcal{T}^{\text{tri}}_{\text{scratch}}\right\}_{\xi'_2} \\ =&\mathcal{F}\left\{A_{\text{scratch}}\,\text{rect}\left(\frac{b}{W}\right)\cdot e^{2\pi i(\gamma_i+\gamma)D/\lambda\,(1-|\frac{b}{W/2}|)}\right\}_{\xi'_2} \\ =&B\cdot\left(1-e^{\pi i(\xi'_2-\frac{2D(\gamma_i+\gamma)}{\lambda})}\right) \\ &+C\cdot\left(e^{-\pi i(W\xi'_2+\frac{2D(\gamma_i+\gamma)}{\lambda})}-1\right)\end{aligned} \tag{29}$$

with

$$B = A_{\text{scratch}}\,\frac{i\,\Phi_D}{2\pi(\xi'_2-\frac{2D(\gamma_i+\gamma)}{W\lambda})} \tag{30}$$

$$C = A_{\text{scratch}}\,\frac{i\,\Phi_D}{2\pi(\xi'_2+\frac{2D(\gamma_i+\gamma)}{W\lambda})} \tag{31}$$

Received May 2017; final version September 2017